Snow effects on altimeter waveform over sea ice in the Weddell Sea

Lu Zhou[1], Henriette Skourup[1], Sahra Kacimi[1], Stefanie Arndt[1], Weixin Zhu[1], Alek Petty[1], Lanqing Huang[1], Julienne Stroeve[1], and Shiming Xu[1]

[1]Affiliation not available

September 16, 2024

Snow effects on altimeter waveform over sea ice in the Weddell Sea

Lu Zhou, Henriette Skourup, Sahra Kacimi, Stefanie Arndt, Weixin Zhu, Alek Petty, Lanqing Huang, Julienne Stroeve, Shiming Xu

***Abstract*—Snow over sea ice affects the overall radiative balance of the polar region by modulating the planetary albedo and influencing sea ice growth. In satellite altimetry, snow is a major source of uncertainty in sea ice thickness estimates, especially with Ku-band radar altimeters. This is because conventional algorithms assume the primary scattering occurs at the snow/ice interface which may not hold for all snowpacks. In particular, complex snow morphological features, including wet snow and/or ice lenses, can shift the main scattering horizon toward the snow surface. These snow features may be particularly prominent over Antarctic sea ice. This study investigates how the properties of the snowpack in the Weddell Sea influence Ku- and Ka-band altimeter waveforms, particularly in the context of extreme conditions and complex snow stratigraphy. Using an adapted waveform model, we deconvolute radar echoes into contributions from the snow surface, snow volume, and ice surface, employing both least-squares fitting and Convolutional Neural Networks (CNN). Our findings challenge previous default assumptions, revealing that snow-volume scattering is as significant as that from the ice surface. To better characterize the snow scattering effects, we propose an adapted threshold first-maximum retracker algorithm (TFMRA) for CryoSat-2 radar freeboard retrieval, identifying a 70% threshold for ice floe retracking as the most accurate based on Operation IceBridge data. The algorithm, applied in CRYO2ICE campaigns and validated against snow buoy measurements, highlights the critical role of snow in altimeter retrievals. The result is particularly important given the recent unprecedented Antarctic sea ice loss and its application for future satellite missions like ESA's CRISTAL.**

***Index Terms*—CryoSat-2, snow scattering, Ku-band waveform, Antarctic sea ice, sea ice thickness**

I. Introduction

Snow and sea ice in the polar regions provide an important influence on the Earth's climate. They regulate albedo radiative feedback mechanisms and hydrological circulation, freshwater flux, heat and momentum transfer, and significantly affect polar biogeochemical and ecological systems [1]–[3].

Snow plays a crucial role in the remote sensing of sea ice thickness from altimeters. However, it remains a significant knowledge gap and a major challenge in the Southern Ocean due to the complex nature of the snow stratigraphy and the heterogeneity of the underlying sea ice, both of which complicate ice thickness retrievals from radar altimeters. This uncertainty arises from the need for delay correction due to reduced radar propagation speed [4] in snow and the scattering of radar waveforms caused by varying snow morphology.

Satellite radar altimeters transmit a microwave pulse at nadir and record backscattered power as the echo. The shape of those echoes depends on the impulse response, as well as the convolution of the transmitted pulse with the returned echo signal. Over sea ice, the waveform is affected by three main factors: (1) surface topography (surface scattering) [5], (2) radar penetration into the snow surface (volume scattering) [5]–[8], and (3) small-scale roughness of the ice surface [9]. Generally, Ku-band altimeters, such as CryoSat-2 (CS-2), are assumed to have their primary scattering surface located at the snow-ice interface (i.e., ice surface scattering), and thus provides a measure of the ice freeboard height above the local sea surface. This only works if Ku-band signals fully penetrate the snow pack. While this assumption was previously assumed to hold under dry, cold conditions with uniform snow stratigraphy [10], this is not always the case even during Arctic winter condition [**?**]. It is further unlikely to hold in the Antarctic where flooding of the ice freeboard is common, resulting in the formation of snow-ice layers and brine-wetted snow. As a result, complex snow morphological features, like wet snow, ice lenses or basal snow salinity [11], shift the main Ku-band radar reflecting horizon towards the snow surface, conditions that are common in Antarctica [12].

CS-2 radar echoes are sensitive to snow properties, surface roughness, and mixed surface types. Studies [13] have shown that snow and ice surface and volume echoes critically contribute to the total echo, particularly in the presence of liquid water in snow and small-scale ice surface roughness. Compared to Ku-band, the Ka-band radar altimeter (e.g., AltiKa) is much more sensitive to scattering from the air-snow interface and/or the snow volume, which shifts the dominant scattering horizon toward the satellite (lower penetration depth than in Ku-band). Therefore, in the Ka-band, radar echoes primarily originate from surface snow scattering and near-surface snow volume scattering. As a result, snow or total

Manuscript received September, 2024. This work is partially funded by the joint project of INTERAAC co-funded by the National Key Research and Development Program of China (project no. 2022YFE010670) and the Research Council of Norway (grant no. 328957). SX is also partially funded by the National Natural Science Foundation of China (project no. 42030602), and the International Partnership Program of Chinese Academy of Sciences (grant no.: 183311KYSB20200015). (Corresponding author: Lu Zhou)

Lu Zhou is with Institute for Marine and Atmospheric Research, Department of Physics, Utrecht University, Utrecht, Netherlands.

Henriette Skourup is with Department of Geodesy and Earth Observation, National Space Institute, DTU Space, The Technical University ofDenmark (DTU), Denmark.

Sahra Kacimi is with Jet Propulsion Laboratory, California Institute of Technology, Pasadena, CA, USA.

Stefanie Arndt is with Alfred-Wegener-Institut, Helmholtz-Zentrum für Polar- und Meeresforschung, Germany.

Weixin Zhu and Shiming Xu are with Department of Earth System Science, Tsinghua University, Beijing, China.

Alek Petty is with University of Maryland, ESSIC, College Park, USA.

Lanqing Huang and Julienne Stroeve are with Earth Sciences, University of College London, London, UK.

freeboard (hereafter noted as fb_s), which measures the height of the air-snow interface above the local sea surface, is used for estimating sea ice thickness.

However, the complex snow stratigraphy [14] over Antarctic sea ice introduces significant uncertainties in identifying the dominant snow scattering horizon [12]. Therefore, CS-2 data are underutilized for sea ice research in the Southern Ocean, limiting accurate sea ice thickness and volume estimations. Recent studies have investigated the effects of the snow backscatter coefficient in the altimeter waveform-fitting model [7], [15]. Furthermore, [16] uses the static snow backscatter to retrieve the Antarctic snow freeboard. These studies highlight that the actual snow surface backscatter varies regionally and seasonally, with the use of fixed values potentially leading to large freeboard biases, sometimes as significant as $\sim$30 cm in the retrieved snow freeboard from a single waveform.

Laser altimeters, such as NASA's Ice, Cloud, and land Elevation Satellite-2 (ICESat-2: IS-2) [17], capture backscatter signals at or near the air-snow interface, above the elevation of the CS-2 signal [18], providing higher-resolution data and more precise estimates of snow-covered ice surface height (or snow freeboard) compared to CS-2 [19]. The CRYO2ICE campaigns (CS-2/IS-2 Resonance Campaign, [20]), which reconcile CS-2 and IS-2 backscatter data, aim to understand how different snow and sea ice properties impact the signals received by satellite radar and laser altimeters [21]. Therefore, effective snow scattering is crucial for accurate ice thickness estimation in both Ku- and Ka-band altimeters, making snow a key factor in accurately estimating sea ice mass balance. This is especially important considering the unprecedented sea ice loss in the Antarctic region over the past seven years, with 2023 reaching a record low.

Here, instead of directly modeling the backscattering properties of snow, this work aims to explore the effects of snow scattering on Ku-band altimeter data, combined with various airborne and in-situ observations. By employing a waveform deconvolution model to analyze CS-2 and Ka-band altimeters (Sec. III), we retrieve the snow surface and volume backscattering coefficients over sea ice in the Weddell Sea and compensate for volume scattering effects in CS-2 retrievals in the Antarctic region. Furthermore, by tuning the threshold in CS-2 echo waveform retracking based on airborne measurement, we determine a robust algorithm for CS-2 freeboard retrieval in Sec. IV-B. Finally, under the current CRYO2ICE framework, this study further explores appropriate algorithms for sea ice thickness retrieval over the Antarctic, providing a new perspective on the region's total sea ice loss (Sec. IV-C1). We also discuss the uncertainties in snow depth from the proposed algorithms in Sec. IV-C2 and the implications of snow scattering effects for future altimeter missions in Sec. V.

II. Data

A. KAREN in CryoVEx Campaign

To investigate the effects of snow scattering, we analyzed data from the MetaSensing Ka-band (34.525 GHz) radar altimeter (KAREN) collected in the Weddell Sea during the CryoSat Validation Experiment (CryoVEx) Antarctic campaign, spanning December 2017 to January 2018 [22]. The CryoVEx campaign dataset included scanning lidar, Ku- and Ka-band nadir-looking radars, and auxiliary imagery, providing critical validation for both CS-2 and the French-Indian Ka-band radar altimetry mission, AltiKa. We applied a deconvolution algorithm to the multi-look power waveforms derived from processed Level 1c (multilooked) data, which typically have a footprint size of 5 m along-track and 12 m across-track. Documentation on the KAREN altimeter's processing chain and file formats can be found at https://doi.org/10.5270/ESA-628233c.

B. NASA's Operation IceBridge (OIB)

To ascertain the airborne snow and sea ice conditions over the Weddell Sea as a reference for CS-2 data, we analyzed data from four NASA's OIB campaigns, which include equipment such as the Airborne Topographic Mapper (ATM) Laser Altimeter, Digital Mapping System (DMS), and Snow Radar. Our analysis utilizes (1) OIB wide swath ATM L1B Elevation and Return Strength dataset [23] to determine surface elevation, featuring ATM spot elevation measurements (approximately 1–2 m footprint) across a 250 m swath over sea ice; (2) DMS L1B Geolocated and Orthorectified Images [24] for detecting sea surface references; (3) L2 elevation data (80 m sample width by $\sim$60 m along track) from IceBridge ATM L2 Icessn Elevation, Slope, and Roughness, Version 2, which are re-sampled and averaged from ATM L1B data [25]; and (4) L1B Radar Echo Strength Profiles dataset [26] from the snow radar for snow depth calculations. The methodology for retrieving snow freeboard (fb_s) and snow depth (h_s) from OIB is detailed in Sec. III-C. To reduce uncertainties from within ice ridges and ensure consistency in detecting open water surfaces (i.e., leads) as local sea level references, both fb_s and h_s are further smoothed over a 10 km interval in the following analysis.

C. CryoSat-2

We adopted the ESA's CS-2 satellite Baseline-E (Baseline-E handbook) L1b waveform and L2 data over the Weddell Sea, acquired by CS-2 synthetic aperture radar altimeter (SIRAL) operating in Ku-band around 13.6 GHz [27].

For CS-2, the pulse-limited footprint in the across-track direction is approximately equal to 1.65 km, while in the along-track direction it is approximately equal to 305 m. Compared to the previous baseline, Baseline-E improves the accuracy and reliability of the data, e.g., by filtering out the outliers in sea surface height anomaly. In this study, each CS-2 L1b file is processed according to established methods introduced in the following.

Here, several CS-2 passes were strategically selected to align with the KAREN-CryoVEx and OIB campaigns, as well as specific ICESat-2 tracks. The geolocations and details of the various instruments used are provided in Fig. 1 and Table 1. In addition to L1b waveforms, this study incorporates total backscattered power, surface scattering coefficient, waveform stack standard deviation, and other relevant parameters from the Baseline-E product to analyze ice surface characteristics

and optimize freeboard retrieval methods. Specifically, L1b waveform data from tracks on January 2, 2018, and January 15, 2018, are utilized to compare deconvolution results with KAREN data, filtered by concurrent Sentinel-1 imagery. Further analyses include data from October 28, 2010; October 13, 2011; November 8, 2012; and October 16, 2014, to refine threshold settings using undertracked OIB ATM and snow radar-derived datasets. Additionally, 46 CS-2 ground tracks, each spanning over 1,000 km and recorded between 2020 and 2022, are included to assess snow and ice conditions along dedicated CRYO2ICE tracks.

Furthermore, L2 radar freeboard (fb_r) from ESA Baseline-E is chosen to compare the fb_r from different algorithms. The Baseline-E fb_r was derived using a 70% threshold-of-first-peak re-tracker over diffuse waveforms and model-fitting peak-finder method for specular echoes [28].

D. ICESat-2

To characterize Antarctic snow and sea ice conditions along CRYO2ICE campaigns, we utilized the snow freeboard (fb_s) from Sea Ice Height ATL07 Version 6 datasets based on the Advanced Topographic Laser Altimeter System (ATLAS) [29] onboard IS-2 during the austral winter months (May to November) between 2020 and 2022 in the Weddell Sea [30]. We selected 46 CRYO2ICE tracks where the time gap between CS-2 and IS-2 measurements was within three hours. IS-2 provides elevation data using three beam pairs (strong and weak beams), with an across-track spacing of approximately 3.3 km between each beam pair and a pair spacing of 90 m. The along-track sampling interval of each beam is 0.7 m with a nominal diameter footprint of 17 m [31]. This study averages the IS-2 fb_s from six beams over 10 km track segments and aligns these measurements with CS-2 fb_r retrievals within the same segment.

E. Sentinel-1B

To visually distinguish surface features over the Weddell Sea during the CryoVEx/KAREN campaign, we analyzed backscatter intensity data from Sentinel-1B (S1B) EW (Extra Wide-swath) Level-1 GRD (Ground Range Detected) MR (medium resolution) Product in dual polarizations (HH+HV) from January 1 and 15, 2018. The Sentinel-1 mission employs a C-band Synthetic Aperture Radar (SAR) operating at 5.405 GHz. The EW mode has been widely used in sea ice monitoring applications thanks to its large spatial coverage (a swath width of 410 km) and medium square spatial resolution of 90 m and square pixel spacing of 40 m. The acquisition times for S1B on January 1, 2018, were between 23:56 and 23:57, while CS-2 navigated the region from 13:25 to 13:30, resulting in a time difference of approximately 10.5 hours. On January 15, 2018, the time gap was much smaller, as Sentinel-1B passed the area between 00:37 and 00:38, closely following CS-2, which traversed the same region from 00:31 to 00:36.

In this study, the SNAP, a software provided by ESA for processing Sentinel data, is used to process the S1B EW GRDM L1 data. This includes radiometric calibration, speckle filtering, geometric ellipsoid correction, conversion to decibel value (dB), and data mosaicking (if multiple images are available in one day). Radiometric calibration (σ_0) is used to convert the original number to backscatter coefficients. The "single product speckle filter" module in SNAP is used to remove speckle noises in images, applying the Lee Sigma filter at a target window size of 3×3 pixels for fine details. The S1B EW GRD SAR data are available in the ESA Open Access Hub here https://scihub.copernicus.eu/dhus/#/home.

F. Snow buoy

To more accurately depict the actual snow accumulation and validate the results from CRYO2ICE tracks over the Weddell Sea, we selected snow depth data from two snow buoys, 2020S55 and 2021S114. These buoys were specifically chosen due to their concurrent geolocation with CRYO2ICE tracks and their coverage of the austral freezing seasons in 2021 and 2022. As listed in [32], the buoy is equipped with four ultrasonic range finders, thus the distance to the surface is measured in hourly intervals, and then the snow depth results from those distance and absolute measurements under each sensor during deployment. Furthermore, to distinguish between actual snow depth and potential snow ice thickness, adjustments were made to account for superimposed ice formation within the snowpack from buoy snow accumulation measurements [33]. Detailed methodologies for snow depth extraction from these buoy measurements are documented in [32], [33]. Snow depth datasets from snow buoys are obtained from https://www.meereisportal.de.

III. Deconvolution and retracking of CS-2 waveform

A. Deconvolution

The received radar echo ($P_r(\tau)$) in the CS-2 L1b data product can be expressed as the convolution of the compressed transmit pulse $P_t(\tau)$ as a function of time (τ), the surface height probability density function ($p(\tau)$), the rough surface response ($I(\tau)$), and scattering cross section per unit volume ($v(\tau)$) [5], [7], [9], [15], [34]:

$$P_r(\tau) = P_t(\tau) \circledast I(\tau) \circledast p(\tau) \circledast v(\tau) \tag{1}$$

In this paper, we used the multi-looked echo waveform model FBEM (Facet-Based numErical Model) from [15] to fit the CS-2 normalized waveform (see their Eq. 8 for more details). This model calculates a stack of N_b received echoes from a prescribed rough surface using the radar equation. Furthermore, following [15], [34], the location of the sea ice layer is defined as $\tau = 0$, as this represents the desired location of our tracking point. And $v(\tau)$ is defined in terms of physical parameters including the surface backscatter coefficients of snow and ice, σ^0_{s-s} and σ^0_{s-i}, respectively, and the integrated volume backscatter of snow and ice, σ^0_{v-s} and σ^0_{v-i}, respectively. Thus, for Antarctic sea ice with thick snow condition, $v(\tau)$ is written as:

$$v(\tau) = \begin{cases} 0, \tau < -\frac{2h_s}{c_s} \\ \sigma^0_{s-s}\delta(\tau + \frac{2h_s}{c_s}) + \sigma^0_{v-s}k_{e-s}\exp[-c_s k_{e-s} \\ (\tau + \frac{2h_s}{c_s})], -\frac{2h_s}{c_s} \leq \tau < 0 \\ \sigma^0_i k^2_{t-s}\exp[-\frac{k_{e-s}h_s}{2}]\delta(\tau), \tau \geq 0 \end{cases} \quad (2)$$

where k_{e-s} the two-way extinction coefficients of snow, c_s the reduced speed of light within the snowpack (obtained from [35]), and h_s the snow depth. Together, these parameters describe the scattering behavior of the snowpack and allow for the estimation of the radar penetration depth, $\frac{1}{k_{e-s}}$, defined as the inverse of the extinction coefficient [36]. For simplicity, we neglect the volume scattering effects from ice σ^0_{v-i} due to the lowest value among the scattering effects, and it remains constant in the previous studies [7], [8].

Here, instead of simulating snow/ice scattering and topography in the waveform fitting model as done by [15], we treat the snow and ice scattering coefficients as unknown parameters. We also keep certain parameters constant in Eq. 8 from [15], such as surface roughness, which is set to 0.2 m (with a range from 0.01 for a very smooth surface to 0.4 for a rough surface). Thus, the deconvolution model and $v(\tau)$ are adapted to include five free parameters: σ^0_{s-s}, σ^0_{s-i}, σ^0_{v-s}, h_s, and k_{e-s}.

1) Waveform deconvolution in fitting routine: Firstly, we fit the modeled waveform to the CS-2 signal using the bounded trust region Levenberg-Marquardt algorithm. As stated in [5], [7], this fitting process iteratively adjusts the model input parameters, minimizing the difference between the modeled waveform and the CS-2 L1B waveform data until a convergence criterion is met or the maximum number of iterations is reached. An initial estimate for each of the free parameters, along with specified upper and lower bounds, is provided to the fitting routine. This approach ensures that the solution closely approximates the physical characteristics of the system.

As mentioned in [7], [34], the waveform deconvolution fitting model is sensitive to the initial guess and bounded provided, so physically realistic values are used as the initial guesses. Following ideas from [8], [34], the initial guess (bounds) for σ^0_{s-s}, σ^0_{s-i}, σ^0_{v-s}, h_s, and k_{e-s} are set to -15 (-20∼5) dB, -1 (-11∼15) dB, -11 (-16∼5) dB, 0.1 (0∼1) m, 0.1 (1e-5∼10) m^{-1}, respectively.

Following [7], we use the squared norm of the residual ("*resnorm*") as a metric for the goodness of fit. Normalized waveforms with a resnorm less than or equal to 0.3 are considered good fits, allowing the extraction of the five free parameters. If the *resnorm* indicates significant error, changes to the initial guess are made, with the fitting process repeating up to 300 iterations. If the *resnorm* remains high after these iterations, the echo is excluded from fb_r retrieval, and the deconvolution of all free parameters is set as NaN values. As found in [7], larger residuals (less valid waveforms) are consistently located around the ice edge and near the continent, such as in the inner Weddell Sea. Subsequently, the five parameters are obtained after several constrained final fits. However, the threshold of 0.3 for the *resnorm* indicates that further work is needed to improve the goodness of fit and reduce errors in the modeled waveform shape.

2) Waveform deconvolution in Convolutional Neural Network (CNN) routine: The traditional deconvolution fitting method described above is computationally intensive due to non-linear iterations and the need for changing initial guesses. To streamline the deconvolution process and enable real-time feedback during training, we introduce a supervised CNN method to further characterize snow scattering properties.

The CNN employed in this study comprises a sequence of layers designed to effectively process and analyze the waveform echo data. The network begins with an input layer that receives the data formatted to specific spatial dimensions. Our CNN is set up with five repetitions of the block unit: 2D convolution, batch normalization (BN) activation, and rectified linear unit (ReLU), and 2D max pooling. This sequence is followed by a 50% dropout layer to prevent overfitting. Fully connected layers then transform the extracted features into formats suitable for regression analysis, concluding with a dense layer that performs regression onto a 1D vector. This final layer includes five neurons, each corresponding to a distinct target variable.

Simulations from the FBEM are specifically used to train and test the CNN configurations, utilizing a consistent surface roughness height of 0.2 m and a large-scale correlation length of 5 m. This approach ensures that the CNN is trained on near-realistic and consistent data, improving its ability to accurately characterize snow properties from the waveform data. A total of 40,000 waveforms generated from FBEM-based simulations were used for CNN training, validation, and testing. Further details on the CNN architecture and model evaluation can be found in Appendix A.

B. Threshold-based wavefrom retracking

To derive the fb_r and thickness from L1b radar waveforms, retracking is necessary to obtain accurate ice surface elevation. This study adopts the threshold first-maximum retracker algorithm (TFMRA), where the retracking point is fixed to the position at which the received power reaches a certain level relative to the first peak of the waveform [37], [38]. This approach is easy to implement, computationally efficient, and robust across various ice surface types.

TFMRA is utilized here to adjust and refine the radar freeboard algorithm, incorporating snow scattering effects. Initially, we refine the CS-2 fb_r values by revising the sea ice floe threshold within TFMRA, specifically in the context of CS-2-OIB undertracks. The revised threshold is then applied to constrain snow depth along the CRYO2ICE tracks and will be compared against existing CS-2 fb_r products.

C. Sea ice thickness and snow depth from OIB ATM and snow radar sensors

To match the freeboard over CS-2-OIB undertracks, fb_s retrieval from ATM and snow depth from snow radar over OIB campaigns must be determined. Limited by the availability of ATM and snow products in IceBridge L4 Sea Ice Freeboard, Snow Depth, and Thickness, Version 1 (IDCSI4) [39], we adjust the fb_s algorithm from ATM as referenced in [40].

Specifically, we derive fb_s by combining ATM L1B and DMS datasets. That is, lead shots and detections are determined when either (i) ATM L1B reflectivity value (R) is $\leq$ 0.25; or (ii) leads are detected from DMS images. The ATM L2 data are then processed with geoid correction by subtracting the DTU 15 Mean Sea Surface Height (MSSH) [41] and are used to calculate fb_s by determining the elevation differences between ice floes and lead shots [42]. Snow freeboard is calculated above the sea level reference only when open water or leads are present within a 10 km segment [43].

Snow depths are obtained using the average from Wavelet [44] and Peakiness algorithm [45] available through the open-source pySnowRadar package developed by [46] via: https://github.com/kingjml/pySnowRadar/tree/v1.1.1.

IV. Experimental results and analysis

A. Waveform deconvolution of CS-2 and KAREN L1 data

To eliminate the subsurface mixed features from leads and ice floes, we referred to the SAR images (Fig. 2) to select only the "clean" ice floes for CS-2 and KAREN deconvolution. Any measurements from leads or open water, as identified from SAR images, were excluded from further analysis. To differentiate ice floes from leads and open water, we first investigated features of different surface types using SAR images, coordinated with the surface scattering coefficient (σ_0, in dB) and the waveform Stack Standard Deviation (SSD, in count) from CS-2 L2 data. By manually detecting different polarization recipes in Fig. 2 to optimize the image visually from SNAP pre-processed S1B images, we further filtered out surface features by applying thresholds of $\sigma_0 < 10$ dB and SSD > 25 counts (relative strict criteria compared to [47]). These criteria were used to identify and retain "clean" CS-2 ice floe samples, as shown in Fig. 2.

Waveform samples for one CS-2 footprint, including one CS-2 waveform sample and 64 KAREN waveform samples, are shown in Fig. 3a. The deconvoluted results for σ^0_{s-s}, σ^0_{s-i}, and σ^0_{v-s} are shown in Fig. 3b and 3c. Specifically, the σ^0_{s-i} (-9.2 dB), which is expected to be dominant, is somewhat lower compared to the σ^0_{s-s} (-4.1 dB) and σ^0_{v-s} (-6.7 dB) in the Ku-band CS-2 backscattered signal. Regarding the scattering features in the KAREN signals, as expected, most of the scattering comes from the snow volume (-9.2 dB), with less from σ^0_{s-s} and σ^0_{s-i}. This clearly indicates that, contrary to previous assumptions that the dominant scattering horizon is located at the snow–ice interface, there is significant scattering within the snow layer (snow volume scattering) that plays a critical role in total CS-2 Ku-band radar scattering. As mentioned in [7], [48], particularly over the Southern Ocean, excluding snow scattering effects in CS-2 leads to overestimation of ice freeboard and underestimation of snow depth, which is a primary reason for low confidence in retrievals of ice freeboard over Antarctic sea ice.

Furthermore, based on the S1B and CS-2 parameters for ice floe filtering, 54 "clean" ice floe samples from CS-2 were selected. Subsequently, a CNN-based deconvolution procedure was applied to both CS-2 and KAREN waveforms. The outcomes for different interface scatterings are summarized in Fig. 4, along with the distribution of snow and ice scattering conditions.

First of all, adhering the criteria of *resnorm* being less than 0.3 and fewer than 300 iterations, 40 out of the 54 samples succeeded in the CS-2 deconvolution scheme, while all samples successfully underwent deconvolution using the KAREN signal. Furthermore, the waveform deconvolution results (σ^0_{v-s}, σ^0_{s-s}, and σ^0_{s-i}) for each CS-2 point were compared to the results based on the 64 KAREN sub-footprint samples, accounting for differences in footprint size. Consequently, each scatter point in Fig. 4b represents the mean of 64 KAREN waveforms within a single CS-2 footprint, while the original KAREN deconvolution results are included in the surrounding distribution.

In Fig. 4a, for CS-2, the mean value for σ^0_{s-i} are around -4.7 dB, which is comparable to σ^0_{v-s}. As anticipated, σ^0_{s-s} is smaller than the signals from ice surface and snow volume scattering, at around -11.5 dB. This finding clearly indicates that the impact of snow volume scattering is significantly underestimated compared to ice surface effects under the current conditions. This discrepancy may lead to an overestimation or underestimation of radar freeboard and, consequently, sea ice thickness in the southern Weddell Sea. Therefore, these parameters require careful recalibration before they can be reliably applied to Antarctic sea ice assessments.

On the contrary, in Fig. 4b, the σ^0_{v-s} and σ^0_{s-s} from KAREN are nearly equivalent, both with mean values around -5.1 dB. Conversely, the σ^0_{s-i} from the Ka-band KAREN signal plays a relatively negligible role, with a mean of approximately -9.1 dB, in the total received signal. This result indicates that snow, particularly surface snow, significantly impedes radar signal penetration, with most of the backscattered signals dependent on snow surface and volume scattering.

Hence, we have observed a significant scattering bias due to snow properties affecting the Ku-band signal receiver, highlighting the need to explore feasible methods for mitigating potential snow-related biases. One approach could involve integrating snow scattering effects into the interpretation of signals and the radar freeboard retrieval processes. In the following section, we aim to identify an appropriate scheme for radar freeboard retrieval, compare various algorithms, and validate them against in-situ measurements.

B. Freeboard improvement in CS-2 from OIB undertracks

Newly derived snow freeboard and snow depth over the Weddell Sea from four OIB campaigns are shown in Fig. 5. Compared to the standard IDCSI4 OIB data product (for flight on October 28, 2010), the newly derived snow depth shows greater consistency in the lower latitudes, while some notable discrepancies are observed between 73°S and 72°S. The fb_s derived from DMS and ATM reflectance shows less consistency with the IDCSI4 version, which exhibits more extreme snow freeboard values. Despite these differences, both fb_s and snow depth show a statistical correlation between the newly derived version and the IDCSI4 version.

Among the four campaigns, only the measurements on October 28, 2010, show larger mean values and variability

of snow depth and fb_s at higher latitudes. Generally, the means and standard deviation (STD) of fb_s (and snow depth) over the four years are 0.43±0.20 (0.30±0.15) m, 0.46±0.29 (0.24±0.11) m, 0.36±0.20 (0.30±0.14) m, and 0.51±0.21 (0.40±0.12) m, respectively, with no significant changes over the years. However, we found that lower latitudes can have thick snow conditions, e.g., the mean snow depth north of 60 °S reached 0.45 m along the track on November 7, 2012. Consequently, negative freeboard due to heavy snow is expected, particularly along the 2012 track. Additionally, fb_r is also expected to be quite small (0.01±0.08 m) in 2014 (Fig. 5d), based on statistics provided above.

To further validate the newly derived snow retrieval from OIB, we compared the OIB airborne measurements with in-situ snow buoy data along the 2014 track. Fig. 6 shows the across-track snow depth and ice thickness measurements from the ice mass balance (IMB) buoy in August and September, which preceded the OIB deployment. The IMB buoy recorded an increase in snow depth from 0.43 m in August to 0.49 m in September, and the OIB-derived snow depth of 0.54 m in October (within the latitude band between 69.5°S and 69°S) aligns well with this expected increase. Combined with the September ice thickness of 1.41 m, the radar freeboard fb_r over the first-year ice-covered region is expected to be around -0.3 cm. Therefore, the updated snow depth and fb_s during the OIB campaigns were validated against both the OIB standard version and co-registered IMB buoy measurements. While the airborne observations indicate no significant changes in overall snow and ice conditions, there are notable inter-annual and regional variations. Specifically, the presence of thick snow and shallow or negative fb_r aligns with findings from previous studies [49], [50].

To determine the optimal freeboard retrieval, ice floe retracking thresholds were selected at 40%, 50%, 60%, 70%, and 80%. These thresholds are denoted as TFMRA-40, TFMRA-50, TFMRA-60, TFMRA-70, and TFMRA-80 in Fig. 7. Given the radar's slow propagation through snow, the fb_s was converted into fb_r based on the relationships established by [4], [51], assuming a default snow density of 350 $\mathrm{kg{\cdot}m^{-3}}$. The mean fb_r from four OIB campaigns is approximately 0.06 ± 0.25 m. The TFMRA-40 threshold exhibits a overestimation (positive) freeboard bias of around 0.29 ± 0.25 m, while the TFMRA-80 threshold shows a underestimation (negative) bias of approximately -0.003 ± 0.16 m, as depicted in Fig. 7a.

In addition to the clear discrepancies in fb_r between the OIB and TFMRA-based CS-2 data, it is important to note that there is no direct correlation between them at a 10 km spatial resolution. Similar phenomena have been observed in various studies [52], [53], primarily due to the mismatch in spatial resolution and sensor representation, with OIB having much finer footprints compared to the coarser footprints of CS-2. Consequently, the comparisons between CS-2 and OIB radar freeboard products focus on the systematic differences between the two. The inconsistencies in grid-scale freeboard validation and comparison between airborne and spaceborne measurements suggest that the bias remains within the estimated range of uncertainty.

The bias and inconsistency between OIB and CS-2 estimates could also be attributed to the OIB snow depth and snow freeboard algorithms used [54], [55], as well as the retracking and roughness effects applied in the CS-2 product [56]. Therefore, a consistent and rigorous approach for extracting and comparing ice conditions is crucial for accurate sea ice retrieval from satellite data and for the assimilation of sea ice information into current climate and coupled models.

To identify the most appropriate freeboard algorithm, we further analyzed the bias derived from OIB data and various retracking thresholds, as shown in Fig. 7b, along with the publicly available ESA Baseline-E product, indicated in red. It is evident that as the retracking threshold for ice floes increases, the absolute bias initially decreases and then increases again as the threshold approaches 80%. We found that the current ESA Baseline-E product, which closely aligns with the TFMRA-50 results, overestimates fb_r by approximately 0.13 m.

Notably, the TFMRA-70 threshold exhibits the smallest bias (approximately 0.002 m) in radar estimation compared to the other thresholds (TFMRA-40: -0.22 m, TFMRA-50: -0.14 m, TFMRA-60: -0.06 m, TFMRA-80: 0.06 m). Therefore, for the CRYO2ICE campaigns, we have selected TFMRA-70 as the optimal algorithm for CS-2 retrieval in the Weddell Sea region.

C. Snow effects over the CRYO2ICE campaigns

1) Snow depth determination: Building on the CS-2 algorithm based on the choices discussed above, we next examine its impact on snow depth retrievals using dual laser and radar altimetry (LaRa) from CRYO2ICE campaign data. Given the different operational modes of CS-2 (Ku-band) and IS-2 (Laser), snow depth is derived from 46 CRYO2ICE tracks by combining near-concurrent (within a three-hour time gap) CS-2 fb_r and IS-2 fb_s measurements. Specifically, snow depth is calculated by subtracting the CS-2 TFMRA-70 fb_r from the six-beam averaged fb_s from IS-2 ATL07 (denoted as ATL07 - TFMRA-70).

Thus, Fig. 8 presents our estimates of snow depth from LaRa over the Weddell Sea during the 2020-2022 period. In addition to the approach used here, i.e., ATL07 - TFMRA-70, snow depth estimates from other methods are also included, namely ATL07 - Baseline-E and ATL07 - TFMRA-50. Firstly, the mean and STD of snow depth for each algorithm are as follows: 0.23 ±0.12 m for TFMRA-70, 0.13±0.09 m for Baseline-E, and 0.14±0.11 m for TFMRA-50. In conclusion, the Baseline-E and TFMRA-50 algorithms yield similar snow depth estimates, while the TFMRA-70 algorithm results in a higher mean and greater variability in snow depth. We also compared the snow depth results across the three years and did not find any significant trends or differences in the mean or variability of snow depth over the 2020-2022 period (see appendix). However, these results highlight the importance of selecting an appropriate algorithm for accurate snow depth retrieval, considering the distinct characteristics and performance of each method.

Given the discrepancies in the snow depth retrieval by using different algorithms, we further employed these snow depth estimates in the sea ice thickness retrieval across all 46 CRYO2ICE tracks. The resulting ice thicknesses from the

above three algorithms are 1.17 $\pm$ 0.99 m for TFMRA-70, 1.67 $\pm$ 1.0 m for Baseline-E, and 1.74 $\pm$ 1.1 m for TFRMA-50. As mentioned previously, a 10 cm underestimation in snow depth can result in an overestimation of ice thickness by more than 0.5 m in the Weddell Sea. This strongly suggests that current ice thickness remote sensing products may contain significant uncertainties and biases due to snow cover, which could obscure the true signal of Antarctic sea ice mass changes.

Therefore, we conclude that current mean sea ice thickness in the Weddell Sea, is likely around 1.2 m, which is noticeably thinner than the 1.4 m recorded by buoy measurements in 2014. Given the 10 cm discrepancy in snow depth between the Baseline-E and the suggested algorithm, it is urgent to revisit CS-2 sea ice thickness and volume changes over the past 14 years in Antarctica. This understanding is particularly crucial in light of the abrupt ice loss observed over the past five years.

Considering the limitations in sensitivity and accuracy of current CS-2 algorithms, it is imperative to develop more innovative, bottom-up retrieval algorithms. Additionally, a comprehensive network of in-situ and airborne measurements should be urgently established and implemented to accurately capture the actual changes in Antarctic sea ice. This will enhance our understanding of its implications for the Southern Ocean and its interactions with ice shelves.

2) Snow depth uncertainties: To further compare and explore the resolved algorithms and results, we co-located four CRYO2ICE tracks with near-concurrent snow buoy deployments. Notably, there was no snow buoy within 2 km of the exact CRYO2ICE acquisition times. Therefore, when aligning the snow buoy and CRYO2ICE data, we coarsened the temporal resolution from sub-daily to bi-weekly (day of CRYO2ICE acquisition $\pm$ 7 days) and the spatial resolution from 2 km to 20 km. Details are provided in Fig. 9, including combined 10 km IS-2 and different versions of CS-2 fb_r, snow depth from the updated CRYO2ICE algorithm, and snow buoy data adjusted for snow-ice formation [33]. Additionally, the STD of IS-2 products within 10 km is shown in the shading.

Generally, both fb_r and fb_s show no latitude dependencies, however, we saw a band with high mean and variability of fb_s in Fig. 9 (a and b). However, IS-2 missed some regions in May 2021 and June 2022 due to insufficient photon detection. Additionally, the derived snow depths from IS-2 and TFMRA-70 confirmed the occurrence of extreme snow conditions, with snow accumulation exceeding 0.7 m at 64^{o}S, contrasting with the thinner snow cover typically observed in Arctic conditions [57], [58]. Some negative snow depths were also noted due to larger fb_r compared to fb_s. One possible explanation is the misalignment of geolocations between CS-2 and IS-2, caused by ice drift and differences in acquisition times. a 3-hour time difference between CS-2 and IS-2 could result in approximately 1 km (0.6 km) of ice drift, assuming high ice speeds of 0.095 ms^{-1} [59] or median speeds of 0.057 ms^{-1} [60]. Another potential reason could be the significant uncertainties related to the detection of both fb_r and fb_s. Even within the same track, snow variability is substantial. For example, the maximum snow depth in June 2022 (Fig. 9c) was around 0.61 m, while the mean was only 0.24$\pm$0.13 m.

Furthermore, snow measured by in-situ buoy measurements was generally thicker than satellite-derived estimates, with most snow depths exceeding 0.6 m (0.66, 0.59, 0.60, and 0.66 m, respectively). While thick snow (over 0.58 m) was observed in satellite data for May 2021 and June 2022 tracks, the comprehensive mean of corresponding ATL07 - TFMRA-70 snow depths were 0.37, 0.23, 0.14, and 0.14 m, respectively. The derived snow depth combining IS-2 fb_s with the upper and lower 25% percentile of TFMRA-70 fb_s is shown in light green shading in Fig. 9. Thus, the snow at the upper boundary increased to 0.58, 0.35, 0.21, and 0.30 m near the buoy measurement locations. Nonetheless, snow depths from CRYO2ICE campaigns were generally shallower than those from in-situ buoy measurements, regardless of the region.

The discrepancies between snow buoy and CRYO2ICE results are further analyzed in Fig. 10, which shows the temporal snow accumulation over 31 days centered on the CRYO2ICE track acquisition day, along with corresponding spatial fb_r and snow depth. Notably, the variability in both snow and sea ice conditions along the buoy monthly trajectories is negligible for the first three tracks. For example, the mean snow depth (sea ice thickness) remains around 0.58 m (1.4 m) and 0.73 m (1.7 m) in May and July 2021, respectively (Fig. 10 a and b). However, in July 2022, the buoy observed significant growth in snow and sea ice, with snow accumulating from 0.6 m to 0.65 m and ice growing from 1.4 m to 1.51 m, though the initial snow depth was already substantial. Generally, snow over sea ice in the Weddell Sea is uniquely thick, as indicated by buoy measurements. In contrast, the current algorithms for fb_s and fb_r exhibit significant temporal and spatial variability, leading to a noticeable underestimation of snow depth.

Although a 10 cm snow depth would lead to an overestimation of ice thickness by more than 0.5 m (as discussed in Sec. IV-C1), the extreme underestimation of snow appears unrealistic. This is evidenced by the fact that most of the fb_s values from IS-2, which are less influenced by snow properties, are below 0.5 m, with a mean value of approximately 0.42 m along the four tracks shown in Fig. 9. Therefore, the presence of a general 0.6 m snow load over sea ice would likely result in widespread "flooding" over the Weddell Sea. However, few recent snow buoy reports indicate snow inundation. This suggests that the uncertainties and representative scale of snow buoy and in-situ measurements need careful examination before implementing satellite footprint-scale validation for satellite snow product retrieval.

Addressing these underestimations in the CRYO2ICE campaigns requires several actions: (i) precise co-geolocation coordination, i.e. sub-daily ice drifting correction, since the geolocation of CRYO2ICE data has not been corrected based on acquisition time in this study; (ii) the development of dedicated algorithms that accommodate temporal or spatial-dependent thresholds for retrieving fb_s and fb_r around Antarctica; (iii) implementing techniques that combine fb_s and fb_r, considering their spatial representation scale, variability, and uncertainties [21]. This could involve initially matching small-scale segments (e.g., less than 10 km) and exploring the potential for integrating data from the two satellites in different

bands.

V. Summary and Discussion

A. Summary

In this study, we address the challenges of retrieving accurate sea ice and snow depth measurements in the Antarctic from CS-2. The thick snow depths on Antarctic sea ice result in significant snow volume scattering effects, which impact the retrieval of radar freeboard (fb_r) from altimeters. The study firstly deconvolutes the CS-2 waveforms and demonstrated the substantial influence of snow volume scattering on radar signals. This scattering has been largely underestimated in previous models, which may have led to discrepancies in freeboard and ice thickness estimates. By incorporating a supervised CNN method, we are able to expedite the deconvolution process, providing real-time feedback and improving the characterization of snow properties. Then, fb_r retrieval from CS-2 based on TFMRA is tuned to better account for snow scattering effects. Additionally, the new snow depth retrievals are validated against in-situ data from OIB campaigns. However, notable discrepancies are observed, particularly at higher latitudes, highlighting the need for further refinement.

Therefore, through our analysis, we identify the TFMRA-70 threshold as the most accurate, minimizing biases in radar freeboard estimates. Lastly, the analysis of CRYO2ICE campaign data, using different algorithmic approaches, reveals significant variability in snow depth and ice thickness estimates. The TFMRA-70 algorithm shows a higher median and greater variability in snow depth compared to other algorithms, indicating its potential for more accurate retrievals. Discrepancies between satellite-derived and in-situ measurements suggest the need for improved co-geolocation coordination and the development of dedicated algorithms that better account for temporal and spatial variability when comparing across different sensors and scales.

The findings highlight the critical role of snow volume scattering in radar signal interpretation and the importance of selecting appropriate algorithms for accurate sea ice and snow depth retrievals. Additionally, there is a need for improved in-situ and airborne measurements. Establishing a comprehensive network of in-situ and airborne measurements will help validate and refine satellite data, thereby enhancing our understanding of Antarctic sea ice dynamics. Lastly, there is an urgent need for the development of advanced algorithms, including innovative bottom-up retrieval approaches, to support current polar climate and coupled models research. All together, these advancements will enhance the reliability of remote sensing products, deepen our understanding of the Antarctic environment, and improve climate change predictions.

B. On the sensitivity/uncertainty

Sensitivity to model parameters of FBEM: The estimation of snow volume scattering (σ°_{s-v}) for CS-2 is highly dependent on the waveform deconvolution and model parameters in FBEM. As shown in Sec. IV-A and Appendix A, surface roughness and decorrelation length significantly influence the simulated waveforms, which in turn affect the quality of the fitting and the derived parameters. To address this, we conducted a sensitivity analysis focusing on the impact of various roughness height (σ), correlation length ($\mathrm{L_{surface}}$), and hurst parameter ($\mathrm{H_{surface}}$) on the deconvoluted snow scattering.

Specifically, within the minimum (Fig. 11c) and maximum (Fig. 11b) combinations of $\mathrm{L_{surface}}$ and $\mathrm{H_{surface}}$, we further select σ in its minimum (0 m) and maximum (1.0 m) values. Then, the resulting differences in σ^0_{s-s}, σ^0_{s-i}, σ^0_{v-s} between the default setting and the sensitivity analysis (i.e., default minus sensitivity) are presented in Fig. 13.

For the 54 waveforms analyzed in Section IV-A, the algorithm successfully retrieved only 11 waveforms in both the minimum and maximum configurations of $\mathrm{L_{surface}}$ and $\mathrm{H_{surface}}$ when surface roughness height (σ) being set to 0 m, significantly fewer than the default setting of 0.2 m. Under higher σ (1.0 m), 17 waveforms were retrieved in the minimum configuration and 34 in the maximum configuration of $\mathrm{L_{surface}}$ and $\mathrm{H_{surface}}$. Fig. 13 illustrates the differences between the default setting and the above minimum and maximum configurations across different σ values. The results indicate that varying $\mathrm{L_{surface}}$ and $\mathrm{H_{surface}}$ introduces only minor discrepancies in scattering, suggesting that correlation length and hurst parameter could remain constant in future studies and settings of Southern Ocean sea ice surface topography and roughness. However, σ^0_{s-s}, σ^0_{s-i}, σ^0_{v-s} exhibit larger variability with higher σ pre-settings, with differences occasionally exceeding 20 dB. Despite these large variabilities, the modes of the deconvolution differences remain centered around 0, indicating robustness in typical parameter settings for Antarctic sea ice studies using the FBEM algorithm.

In summary, under various ice roughness and decorrelation length settings, waveform deconvolution demonstrates significant variability. Surface roughness emerges as the primary contributor to waveform fitting, while other parameters play a secondary or tertiary role. This result also indicates that the snow volume scattering plays a key role in modulating the retrieved CS2 waveforms, and its effects can be well captured by the modified FBEM model. Nonetheless, FBEM provides consistency and confidence in waveform fitting and is expected to have broader applications when incorporating actual surface elevation and roughness information.

Representation issues: Another key source of uncertainty for CS2 waveform retrieval is the highly heterogeneous sea ice cover within the CS2 footprint. The effect of heterogeneity is partially reflected by the deconvolution study with CS2 waveforms and collocating KAREN observations in Sec. IV-A. The waveform model in FBEM assumes homogeneity of all the contributing factors, such as the rough surface response function (I in Eqs. 2) and the height distribution function (p in Eqs. 2). While each footprint of CS2 waveforms covers over 300 by 1500 m^2, that by KAREN is much finer at about $10m^2$. Therefore, the sea ice within KAREN footprints is more homogeneous, resulting in overall much better waveform fittings than those with CS2. On the other hand, various sea ice types (i.e., thin ice, older ice, small open water) may be present within the CS2 footprint, each with its respective snow

properties, surface height distribution, and consequently, the response function. The potential lack of representation is also present during the derivation of snow depth with CRYO2ICE track pairs, since the spatial coverage of CS2 is much larger than IS2 beams. The representation-related uncertainties for both CRYO2ICE and buoy are not accounted for the inter-comparison in Sec. IV-C2, although we do not consider it the source of systematic difference between the two snow depth products.

C. Outlook for altimetry

Retrieval of radar freeboard - historical dataset: The long-term record of Antarctic sea ice thickness and volume relies on satellite altimetry, and the knowledge about the snow's role in modulating the radar waveforms is key to reduce its uncertainty. The limited radar penetration in the snow cover is mainly caused by the complex snow stratigratphy and the surface and volume scattering of the radar signal. When accounting for the snow's roles, the physical waveform simulations of FBEM can be utilized to estimate the key parameters of the snow cover, as shown for "clean" CS2 footprints in Sec. IV-A. Also, the model parameters of FBEM are not generally available, and potentially highly variant, both spatially and temporally. These factors hinder the wide application with FBEM for direct retrieval of these parameters, including snow depth. In order to further improve the CS2-based record of Antarctic sea ice, other independent satellite observations such as radiometers and scatterometers provide complementary capabilities and can be utilized through physical synergy with CS2 [61].

ESA CRISTAL: Furthermore, the future dual-frequency, delay-Doppler radar altimeter of CRISTAL from ESA [62] is planned to launch during the second half of 2020's. Although the along-track resolution of CRISTAL over sea ice is further improved upon CS2, the global and polar climate during its timeframe is expected to be even warmer than CS2 according to current climate projections. While Ka-band radar signal is shown to mainly reflect from the snow's surface, the potential problem of penetration in the snow cover at Ku-band persists, if not worsens. In order to accurately retrieve snow depth and ice thickness with CRISTAL, the snow processes should be effectively accounted for in both Antarctic and Arctic waters.

APPENDIX

As previously mentioned, the CNN ave been employed to decompose and fit the snow and ice scattering coefficients from CryoSat-2 ice floe waveforms. CNN first suggested by [64] and has since been further developed with various structures and algorithms [65]. Numerous studies have utilized CNN approaches for image recognition, classification tasks, and polar sea ice applications, such as sea ice concentration [66], thickness [67], and motion forecasting [68], [69] . Following the methodologies of [68], [69], we implemented the CNN in Python using the TensorFlow Keras library [70]. The architecture includes convolutional and ReLU layers with 3×3 strides and filter sizes., utilizing 'same' padding to maintain dimensionality, and max pooling layers with 2×2 strides

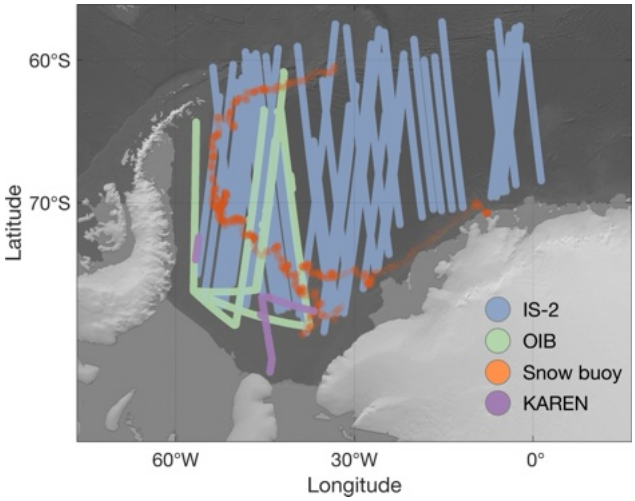

Fig. 1. Geolocation of all observations included in this study; ICESat-2, OIB, snow buoy, and KAREN-CryoVEx

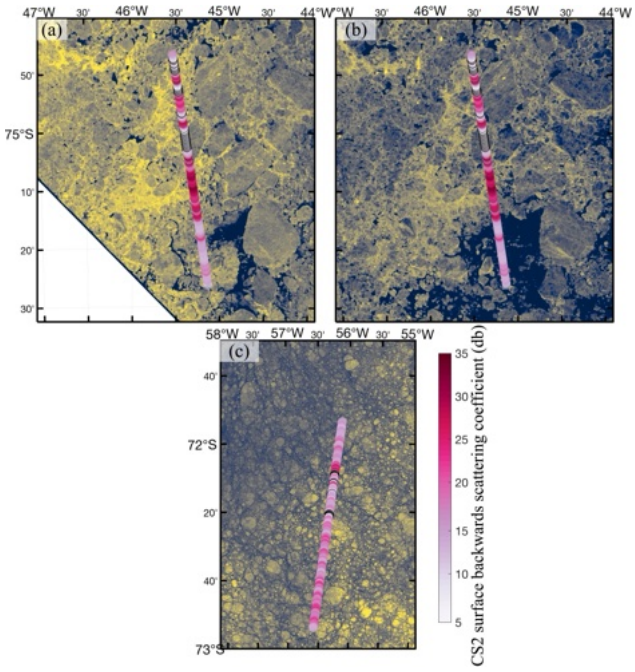

Fig. 2. Concurrent Sentinel-1B SAR HH and HV arithmetical combination images over (a) HH×HV on 01-Jan-2018, (b) HH×HV on 03-Jan-2018 and (c) HV×[2HH + HV×(1 − 2HH)] (green channel generation [63]) 15-Jan-2018 overlaid by the CS-2 radar scattering coefficient (db) from Baseline-E L2 products.

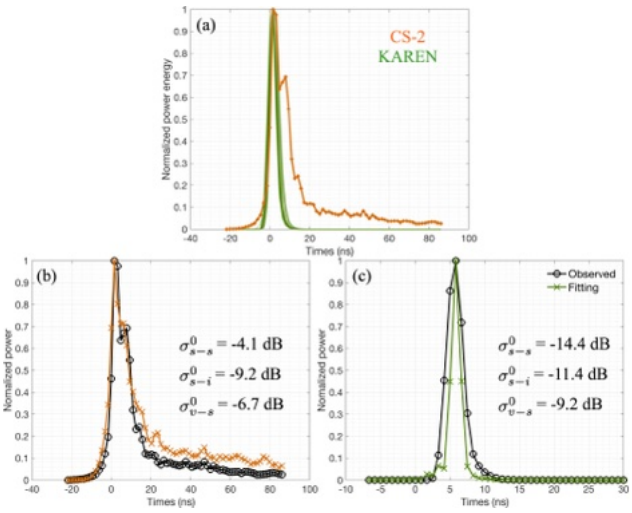

Fig. 3. Within CS-2 footprint (a), one CS-2 waveform (orange) corresponds to 64 KAREN waveform samples (green). The deconvoluted results, including fitted (colored) and actual (black) waveforms for CS-2 (b) and KAREN (c), are shown for a *resnorm* of less than 0.3.

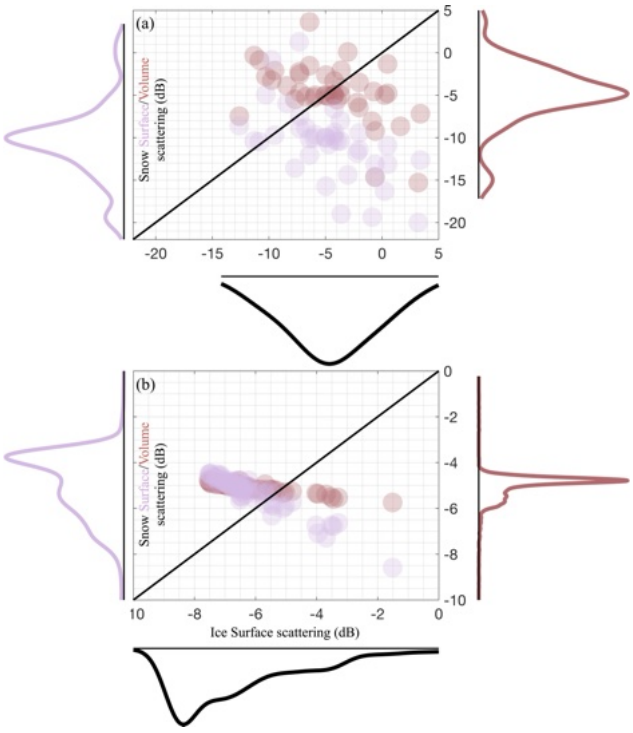

Fig. 4. Summarised ice surface (black), snow surface (purple) and volume (salmon) scattering results from the CNN deconvolution process, based on (a) CS-2 and (b) KAREN waveforms, with *resnorm* less than 0.3.

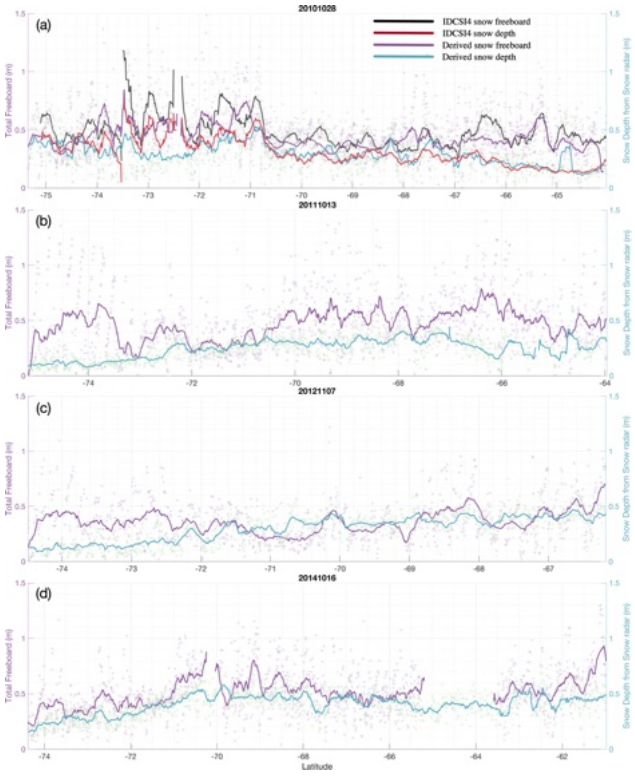

Fig. 5. Snow freeboard (black ones from IDCSI4 product, purple ones from DMS and ATM L2 retrieval) and snow depth (red ones from IDCSI4 product, blue ones from snow radar retrieval) along CS-2-OIB undertrack over (a) 28-Oct-2010, (b) 13-Oct-2011, (c) 07-Nov-2012, and (d) 16-Oct-2014. Dots are original resolution and lines are 10 km running mean.

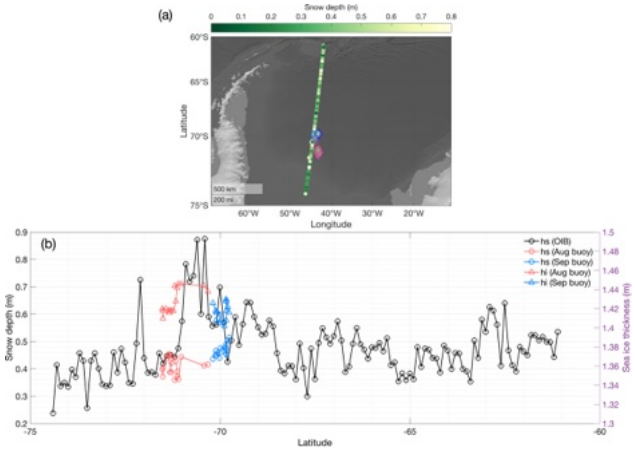

Fig. 6. Snow depth (hs) comparison between OIB campaign on October 16, 2014, and IMB buoy (name: 2014T8) determined during the entire months of August (red) and September (blue) trajectories, along with ice thickness (hi) detection from IMB buoy.

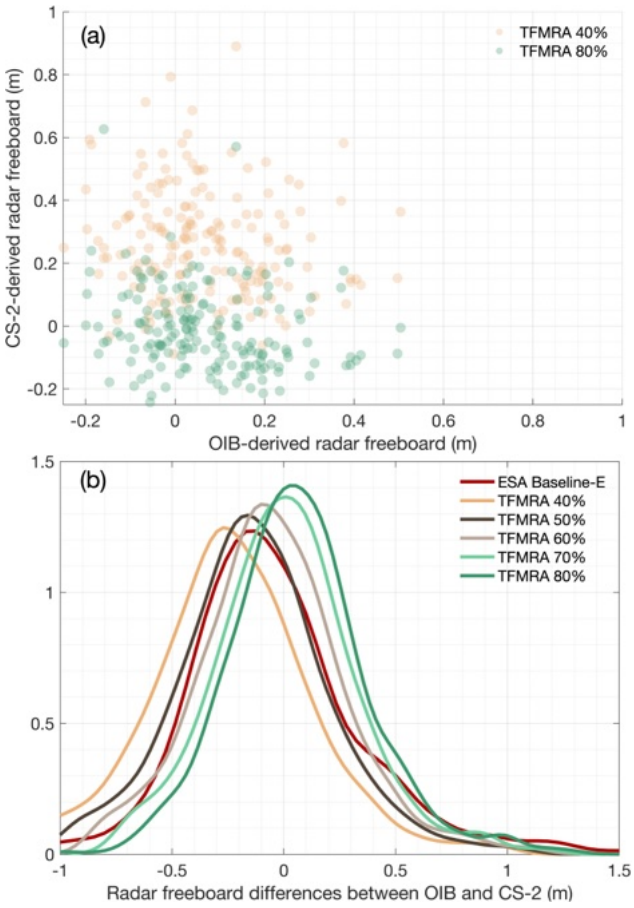

Fig. 7. (a) Comparison of radar freeboard between OIB-derived measurements (snow freeboard and snow depth) and CS-2 retrievals under various TFMRA retracking thresholds. (b) the distribution of discrepancies in radar freeboard derived from OIB and CS-2 using different TFMRA retracking thresholds.

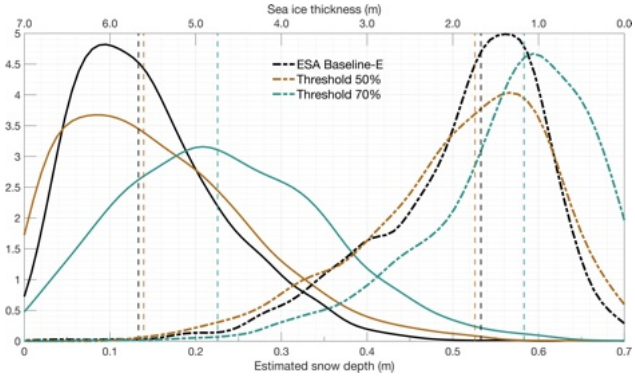

Fig. 8. The distribution of derived snow depth (solid lines), and the mean value (vertical dotted lines) based on the combination of IS2 snow freeboards and CS-2 radar freeboards based on different algorithms (TFMRA-50: brown, TFMRA-70: green, and ESA baseline-E: black) using 46 CRYO2ICE tracks covering three years, 2020-2022. The corresponding sea ice thickness and mean values of the different algorithms (dash-dotted lines) are shown as well.

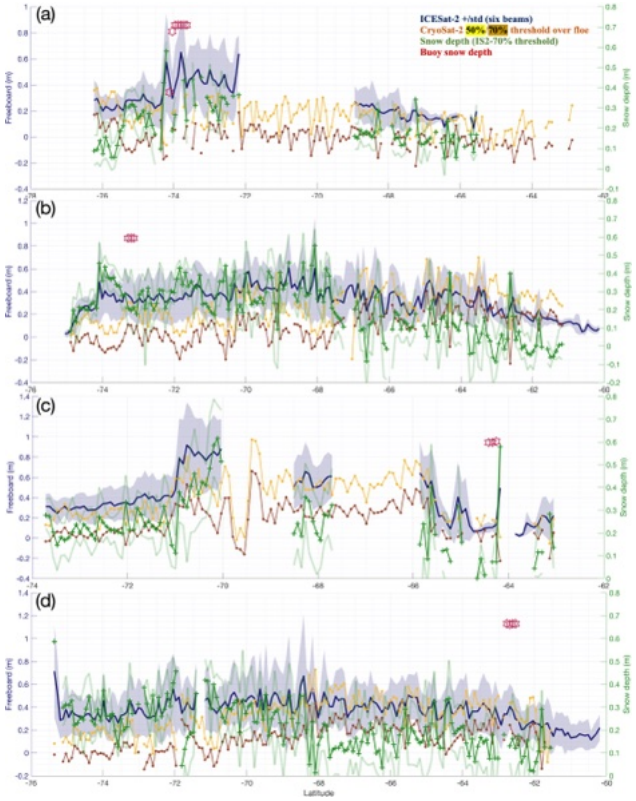

Fig. 9. Mean and one standard deviation in snow/radar freeboard and snow depth in 10 km resolution over four different CRYO2ICE tracks over (a) 29-May-2021, (b) 16-Jul-2021, and (c) 22-Jun-2022 and (d) 03-Jul-2022. Snow freeboard is derived from mean of IS-2 six beams (darked blue); radar freeboard in different colors are obtained from different thresholds (50/70%: orange). Snow depth are extracted from IS2 snow freeboard and TFMRA 70% threshold retracking (green lines) as well as from near-concurrent and -colocation snow buoy (red stars).

and filter sizes.. The network comprises block units with 16, 32, 64, 64, and 128 filters, and training is conducted over 50 epochs with a batch size of 128 (see Fig. A.12 for the network architecture).

n this CNN model, the input data is the waveform derived from Eq.1, given specific values for σ^0_{s-s}, σ^0_{s-i}, σ^0_{v-s}, h_s, and k_{e-s}. Consequently, the output consists of these five parameters. The network's performance is evaluated by comparing the predicted waveform, calculated from the deconvoluted parameters, with the target or ground truth waveform. This involves reinserting the CNN-derived parameters back into Eq.1 to generate the waveform.

Optimization is performed using the Adam optimizer, with a self-defined normalized root-mean-square error (NRMSE: $\sqrt{\frac{\sum (Y_i - X_i)^2}{N}}$), representing the linear fitting results between the target and recalculated waveform, as the loss function. The overall performance of the network is further assessed by computing the NRMSE and R^2 values for waveform fitting across all FBEM-based waveforms, yielding results of 0.11 ± 0.01 and 0.45 ± 0.02, respectively.

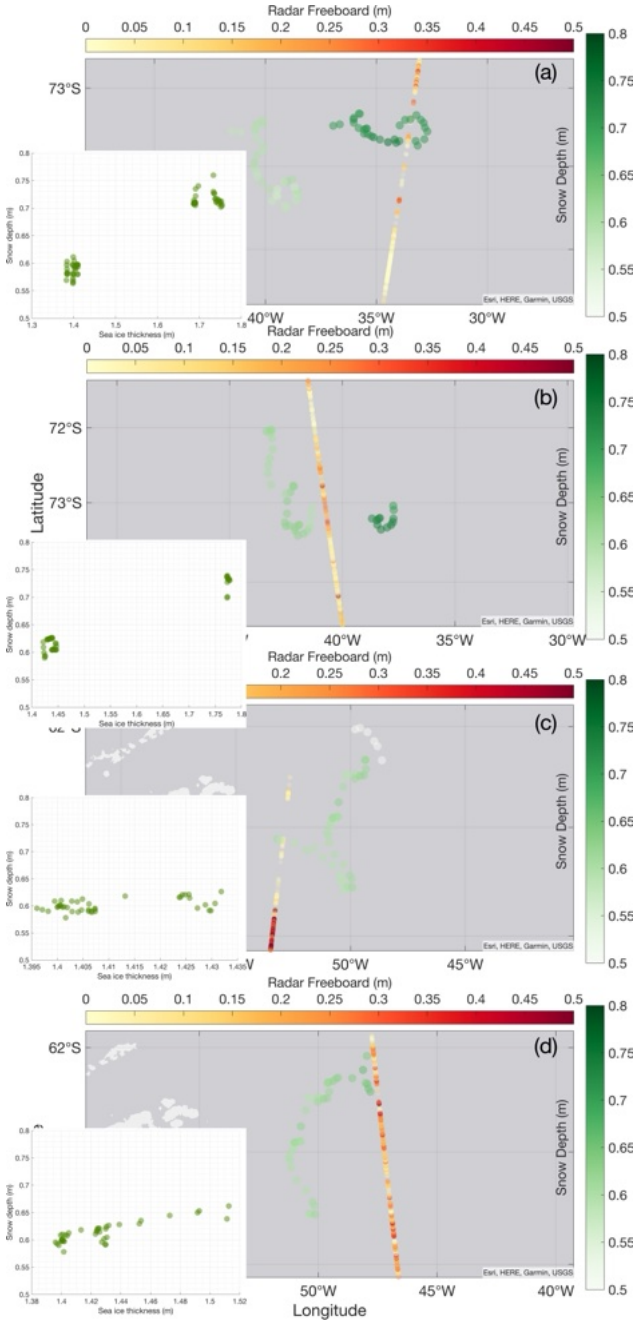

Fig. 10. Geolocation of radar freeboard from CS-2 70% threshold retracking over four different track as mentioned in Fig.9 overlaid by daily snow buoy trajectories over the month.

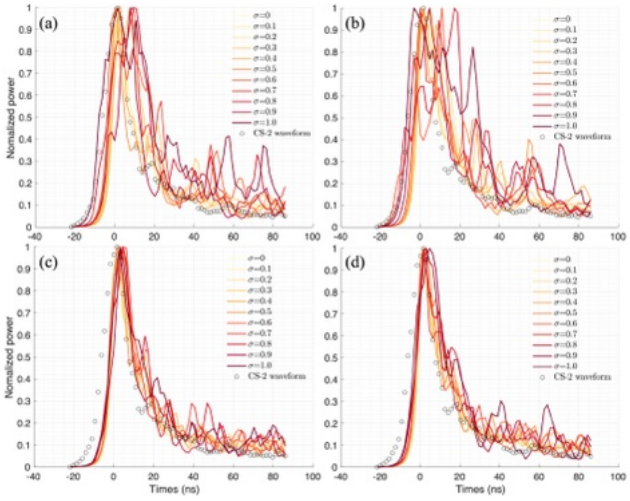

Fig. 11. The waveform simulation (lines) from FBEM with different large-scale roughness height (σ) under different large-scale correlation length ($L_{surface}$: m) and hurst parameter for fractal surface ($H_{surface}$) scenario. (a) $L_{surface}$ = 10m, $H_{surface}$ = 0.01, (b) $L_{surface}$ = 10m, $H_{surface}$ = 1, (c) $L_{surface}$ = 1m, $H_{surface}$ = 1m, $H_{surface}$ = 1. Dots are from CS-2 waveform.

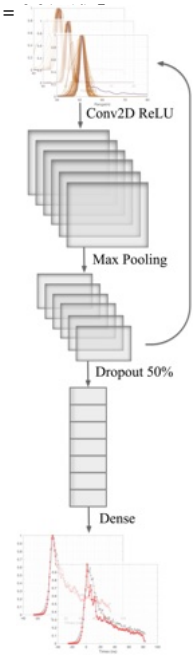

Fig. 12. Geolocation of radar freeboard from CS-2 70% threshold retracking over four different track as mentioned in Fig.9 overlaid by daily snow buoy trajectories over the month.

REFERENCES

[1] B. Loose, L. A. Miller, S. Elliott, and T. Papakyriakou, "Sea ice biogeochemistry and material transport across the frozen interface," *Oceanography*, vol. 24, no. 3, pp. 202–218, 2011.

[2] D. Lannuzel, L. Tedesco, M. Van Leeuwe, K. Campbell, H. Flores, B. Delille, L. Miller, J. Stefels, P. Assmy, J. Bowman *et al.*, "The future of Arctic sea-ice biogeochemistry and ice-associated ecosystems," *Nature Climate Change*, vol. 10, no. 11, pp. 983–992, 2020.

[3] N. S. Steiner, J. Bowman, K. Campbell, M. Chierici, E. Eronen-Rasimus, M. Falardeau, H. Flores, A. Fransson, H. Herr, S. J. Insley *et al.*, "Climate change impacts on sea-ice ecosystems and associated ecosystem services," *Elem Sci Anth*, vol. 9, no. 1, p. 00007, 2021.

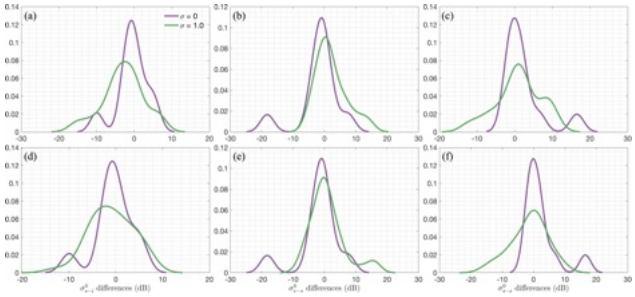

Fig. 13. The differences in in deconvoluted σ^0_{s-i} ((a) and (d)), σ^0_{v-s} ((b) and (e)), σ^0_{s-s} ((c) and (f)) between default setting ($L_{surface}$ = 5m, $H_{surface}$ = 0.5, and σ = 0.2 m) and sensitivity tests. Panels (a), (b), and (c) reflect the configuration of $L_{surface}$ = 1m, $H_{surface}$ = 0.01, while panels (d), (e), and (f) reflect the configuration of $L_{surface}$ = 10m, $H_{surface}$ = 1. The purple and green lines represent the results for surface roughness height (σ) set to 0 m and 1.0 m, respectively.

[4] R. D. Mallett, I. R. Lawrence, J. C. Stroeve, J. C. Landy, and M. Tsamados, "Brief communication: Conventional assumptions involving the speed of radar waves in snow introduce systematic underestimates to sea ice thickness and seasonal growth rate estimates," *The Cryosphere*, vol. 14, no. 1, pp. 251–260, 2020.

[5] T. Slater, A. Shepherd, M. Mcmillan, T. W. Armitage, I. Otosaka, and R. J. Arthern, "Compensating changes in the penetration depth of pulse-limited radar altimetry over the Greenland ice sheet," *IEEE Transactions on Geoscience and Remote Sensing*, vol. 57, no. 12, pp. 9633–9642, 2019.

[6] T. W. Armitage, D. J. Wingham, and A. L. Ridout, "Meteorological origin of the static crossover pattern present in low-resolution-mode CryoSat-2 data over central Antarctica," *IEEE Geoscience and Remote Sensing Letters*, vol. 11, no. 7, pp. 1295–1299, 2013.

[7] S. W. Fons and N. T. Kurtz, "Retrieval of snow freeboard of Antarctic sea ice using waveform fitting of CryoSat-2 returns," *The Cryosphere*, vol. 13, no. 3, pp. 861–878, 2019.

[8] S. Fons, N. Kurtz, and M. Bagnardi, "A decade-plus of Antarctic sea ice thickness and volume estimates from CryoSat-2 using a physical model and waveform fitting," *The Cryosphere*, vol. 17, no. 6, pp. 2487–2508, 2023.

[9] M. P. Makynen and M. T. Hallikainen, "Simulation of ASIRAS altimeter echoes for snow-covered first-year sea ice," *IEEE Geoscience and Remote Sensing Letters*, vol. 6, no. 3, pp. 486–490, 2009.

[10] S. Beaven, G. Lockhart, S. Gogineni, A. Hossetnmostafa, K. Jezek, A. Gow, D. Perovich, A. Fung, and S. Tjuatja, "Laboratory measurements of radar backscatter from bare and snow-covered saline ice sheets," *Remote Sensing*, vol. 16, no. 5, pp. 851–876, 1995.

[11] V. Nandan, T. Geldsetzer, J. Yackel, M. Mahmud, R. Scharien, S. Howell, J. King, R. Ricker, and B. Else, "Effect of snow salinity on CryoSat-2 Arctic first-year sea ice freeboard measurements," *Geophysical Research Letters*, vol. 44, no. 20, pp. 10–419, 2017.

[12] R. C. Willatt, K. A. Giles, S. W. Laxon, L. Stone-Drake, and A. P. Worby, "Field investigations of Ku-band radar penetration into snow cover on Antarctic sea ice," *IEEE Transactions on Geoscience and remote sensing*, vol. 48, no. 1, pp. 365–372, 2009.

[13] M. P. Makynen and M. T. Hallikainen, "Simulation of ASIRAS altimeter echoes for snow-covered first-year sea ice," *IEEE Geoscience and Remote Sensing Letters*, vol. 6, no. 3, pp. 486–490, 2009.

[14] R. A. Massom, H. Eicken, C. Hass, M. O. Jeffries, M. R. Drinkwater, M. Sturm, A. P. Worby, X. Wu, V. I. Lytle, S. Ushio *et al.*, "Snow on Antarctic sea ice," *Reviews of Geophysics*, vol. 39, no. 3, pp. 413–445, 2001.

[15] J. C. Landy, M. Tsamados, and R. K. Scharien, "A facet-based numerical model for simulating SAR altimeter echoes from heterogeneous sea ice surfaces," *IEEE Transactions on Geoscience and Remote Sensing*, vol. 57, no. 7, pp. 4164–4180, 2019.

[16] S. Fons, N. T. Kurtz, M. Bagnardi, A. A. Petty, and R. Tilling, "Assessing CryoSat-2 Antarctic Snow Freeboard Retrievals Using Data From ICESat-2," *Earth and Space Science*, vol. 8, no. 7, p. e2021EA001728, 2021.

[17] T. A. Neumann, A. J. Martino, T. Markus, S. Bae, M. R. Bock, A. C. Brenner, K. M. Brunt, J. Cavanaugh, S. T. Fernandes, D. W. Hancock *et al.*, "The Ice, Cloud, and Land Elevation Satellite–2 Mission: A global geolocated photon product derived from the advanced topographic laser altimeter system," *Remote Sensing of Environment*, vol. 233, p. 111325, 2019.

[18] F. Garnier, S. Fleury, G. Garric, J. Bouffard, M. Tsamados, A. Laforge, M. Bocquet, R. M. Fredensborg Hansen, and F. Remy, "Advances in altimetric snow depth estimates using bi-frequency SARAL and CryoSat-2 Ka–Ku measurements," *The Cryosphere*, vol. 15, no. 12, pp. 5483–5512, 2021.

[19] A. A. Petty, N. Keeney, A. Cabaj, P. Kushner, and M. Bagnardi, "Winter Arctic sea ice thickness from ICESat-2: upgrades to freeboard and snow loading estimates and an assessment of the first three winters of data collection," *The Cryosphere*, vol. 17, no. 1, pp. 127–156, 2023.

[20] M. Ewart, J. Bizon, J. Alford, R. Easthope, N. Gourmelen, A. Horton, A. Incatasciato, T. Parrinello, J. Bouffard, A. Di Bella, T. Goss, and M. Michael, C. anc Meloni, "cs2eo Version 3," 2022. [Online]. Available: https://earth.esa.int/eogateway/missions/cryosat/cryo2ice

[21] R. M. Fredensborg Hansen, H. Skourup, E. Rinne, K. V. Høyland, J. C. Landy, I. Merkouriadi, and R. Forsberg, "Arctic freeboard and snow depth from near-coincident CryoSat-2 and ICESat-2 (CRYO2ICE) observations: A first examination of winter sea ice during 2020–2022," *Earth and Space Science*, vol. 11, no. 4, p. e2023EA003313, 2024.

[22] S. Hvidegaard, R. Forsberg, H. Skourup, M. Kristensen, A. Olesen, A. Olesen, A. Coccia, K. Macedo, V. Helm, R. Ladkin *et al.*, "ESA CryoVEx/KAREN Antarctica 2017-18," 2020.

[23] M. Studinger, "IceBridge ATM L1B Elevation and Return Strength, Version 2," 2013. [Online]. Available: https://nsidc.org/data/ILATM1B/versions/2

[24] R. Dominguez, "IceBridge DMS L1B Geolocated and Orthorectified Images, Version 1," 2010. [Online]. Available: https://nsidc.org/data/IODMS1B/versions/1

[25] M. Studinger, "IceBridge ATM L2 Icessn Elevation, Slope, and Roughness, Version 2," 2014. [Online]. Available: https://nsidc.org/data/ILATM2/versions/2

[26] J. Paden, J. Li, C. Leuschen, F. Rodriguez-Morales, and R. Hale, "IceBridge Snow Radar L1B Geolocated Radar Echo Strength Profiles, Version 2," 2014, [Date Accessed:28-Feb-2022].

[27] D. Wingham, C. Francis, S. Baker, C. Bouzinac, D. Brockley, R. Cullen, P. de Chateau-Thierry, S. Laxon, U. Mallow, C. Mavrocordatos *et al.*, "CryoSat: A mission to determine the fluctuations in Earth's land and marine ice fields," *Advances in Space Research*, vol. 37, no. 4, pp. 841–871, 2006.

[28] K. Giles, S. Laxon, D. Wingham, D. Wallis, W. Krabill, C. Leuschen, D. McAdoo, S. Manizade, and R. Raney, "Combined airborne laser and radar altimeter measurements over the Fram Strait in May 2002," *Remote Sensing of Environment*, vol. 111, no. 2-3, pp. 182–194, 2007.

[29] R. Kwok, A. A. Petty, G. Cunningham, T. Markus, D. Hancock, A. Ivanoff, J. Wimert, M. Bagnardi, N. Kurtz, and the ICESat-2 Science Team., "ATLAS/ICESat-2 L3A Sea Ice Height, Version 6," 2023. [Online]. Available: https://nsidc.org/data/ATL07/versions/6

[30] R. M. F. Hansen, H. Skourup, S. B. Simonsen, I. R. Lawrence, A. Shepherd, J. Li, F. Rodriguez-Morales, R. Forsberg, K. V. Høyland, E. Rinne *et al.*, "CRYO2ICE (CryoSat-2 and ICESat-2) under-flight in the Weddell Sea: sea ice and snow estimates of Antarctic summer sea ice from near-coincident space-and airborne multi-frequency altimetry," *AGU23*, 2023.

[31] L. Magruder, T. Neumann, and N. Kurtz, "ICESat-2 Early Mission Synopsis and Observatory Performance," *Earth and Space Science*, vol. 8, no. 5, p. e2020EA001555, 2021.

[32] M. Nicolaus, M. Hoppmann, S. Arndt, S. Hendricks, C. Katlein, A. Nicolaus, L. Rossmann, M. Schiller, and S. Schwegmann, "Snow depth and air temperature seasonality on sea ice derived from snow buoy measurements," *Frontiers in Marine Science*, vol. 8, p. 655446, 2021.

[33] S. Arndt, N. Maaß, L. Rossmann, and M. Nicolaus, "From snow accumulation to snow depth distributions by quantifying meteoric ice fractions in the Weddell Sea," *The Cryosphere*, vol. 18, no. 4, pp. 2001–2015, 2024.

[34] N. T. Kurtz, N. Galin, and M. Studinger, "An improved CryoSat-2 sea ice freeboard retrieval algorithm through the use of waveform fitting," *The Cryosphere*, vol. 8, no. 4, pp. 1217–1237, 2014.

[35] R. Kwok and G. Cunningham, "Variability of Arctic sea ice thickness and volume from CryoSat-2," *Philosophical Transactions of the Royal Society A: Mathematical, Physical and Engineering Sciences*, vol. 373, no. 2045, p. 20140157, 2015.

[36] R. Arthern, D. Wingham, and A. Ridout, "Controls on ERS altimeter measurements over ice sheets: Footprint-scale topography, backscatter

fluctuations, and the dependence of microwave penetration depth on satellite orientation," *Journal of Geophysical Research: Atmospheres*, vol. 106, no. D24, pp. 33 471–33 484, 2001.
[37] V. Helm, A. Humbert, and H. Miller, "Elevation and elevation change of Greenland and Antarctica derived from CryoSat-2," *The Cryosphere*, vol. 8, no. 4, pp. 1539–1559, 2014.
[38] G. D. Quartly, E. Rinne, M. Passaro, O. B. Andersen, S. Dinardo, S. Fleury, A. Guillot, S. Hendricks, A. A. Kurekin, F. L. Müller *et al.*, "Retrieving sea level and freeboard in the Arctic: A review of current radar altimetry methodologies and future perspectives," *Remote Sensing*, vol. 11, no. 7, p. 881, 2019.
[39] K. N., M. Studinger, J. Harbeck, V. Onana, and D. Yi., "IceBridge L4 Sea Ice Freeboard, Snow Depth, and Thickness, Version 1," 2015.
[40] N. Kurtz and J. Harbeck, "Operation IceBridge sea ice freeboard, snow depth, and thickness data products manual, version 2 processing," *NSIDC, Boulder, CO, USA, Tech. Rep*, 2015.
[41] O. B. Andersen, L. Stenseng, G. Piccioni, and P. Knudsen, "The dtu15 mss (mean sea surface) and dtu15lat (lowest astronomical tide) reference surface," in *ESA Living planet symposium 2016*, 2016.
[42] L. Tian, H. Xie, S. F. Ackley, J. Tang, A. M. Mestas-Nuñez, and X. Wang, "Sea-ice freeboard and thickness in the Ross Sea from airborne (IceBridge 2013) and satellite (ICESat 2003–2008) observations," *Annals of Glaciology*, vol. 61, no. 82, pp. 24–39, 2020.
[43] R. Kwok and S. Kacimi, "Three years of sea ice freeboard, snow depth, and ice thickness of the Weddell Sea from Operation IceBridge and CryoSat-2," *The Cryosphere*, vol. 12, no. 8, pp. 2789–2801, 2018.
[44] T. Newman, S. L. Farrell, J. Richter-Menge, L. N. Connor, N. T. Kurtz, B. C. Elder, and D. McAdoo, "Assessment of radar-derived snow depth over Arctic sea ice," *Journal of Geophysical Research: Oceans*, vol. 119, no. 12, pp. 8578–8602, 2014.
[45] A. Jutila, J. King, J. Paden, R. Ricker, S. Hendricks, C. Polashenski, V. Helm, T. Binder, and C. Haas, "High-resolution snow depth on arctic sea ice from low-altitude airborne microwave radar data," *IEEE Transactions on Geoscience and Remote Sensing*, vol. 60, pp. 1–16, 2021.
[46] J. King, M. Brady, and T. Newman, "kingjml/pySnowRadar: Updated IEEE TGRS Submission," 2020.
[47] S. Lee, J. Im, J. Kim, M. Kim, M. Shin, H.-c. Kim, and L. J. Quackenbush, "Arctic sea ice thickness estimation from cryosat-2 satellite data using machine learning-based lead detection," *Remote Sensing*, vol. 8, no. 9, p. 698, 2016.
[48] S. Paul, S. Hendricks, R. Ricker, S. Kern, and E. Rinne, "Empirical parametrization of Envisat freeboard retrieval of Arctic and Antarctic sea ice based on CryoSat-2: progress in the ESA Climate Change Initiative," *The Cryosphere*, vol. 12, no. 7, pp. 2437–2460, 2018.
[49] S. Schwegmann, E. Rinne, R. Ricker, S. Hendricks, and V. Helm, "About the consistency between envisat and cryosat-2 radar freeboard retrieval over antarctic sea ice," *The Cryosphere*, vol. 10, no. 4, pp. 1415–1425, 2016.
[50] N. Wever, K. Leonard, T. Maksym, S. White, M. Proksch, and J. T. Lenaerts, "Spatially distributed simulations of the effect of snow on mass balance and flooding of Antarctic sea ice," *Journal of Glaciology*, pp. 1–19, 2021.
[51] F. T. Ulaby, R. K. Moore, and A. K. Fung, *Microwave remote sensing: Active and passive. Volume 3-From theory to applications*, ser. Artech House microwave library. Addison-Wesley Publishing Company, Advanced Book Program/World Science Division, 1986, no. v. 3. [Online]. Available: https://books.google.nl/books?id=X9APAQAAIAAJ
[52] D. Yi, N. Kurtz, J. Harbeck, R. Kwok, S. Hendricks, and R. Ricker, "Comparing Coincident Elevation and Freeboard From IceBridge and Five Different CryoSat-2 Retrackers," *IEEE Transactions on Geoscience and Remote Sensing*, vol. 57, no. 2, pp. 1219–1229, 2019.
[53] S. Xu, L. Zhou, and B. Wang, "Variability scaling and consistency in airborne and satellite altimetry measurements of Arctic sea ice," *The Cryosphere*, vol. 14, no. 2, pp. 751–767, 2020.
[54] R. Kwok and C. Haas, "Effects of radar side-lobes on snow depth retrievals from Operation IceBridge," *Journal of Glaciology*, vol. 61, no. 227, pp. 576–584, 2015.
[55] R. Kwok, N. T. Kurtz, L. Brucker, A. Ivanoff, T. Newman, S. L. Farrell, J. King, S. Howell, M. A. Webster, J. Paden *et al.*, "Intercomparison of snow depth retrievals over Arctic sea ice from radar data acquired by Operation IceBridge," *The Cryosphere*, vol. 11, no. 6, pp. 2571–2593, 2017.
[56] J. C. Landy, A. A. Petty, M. Tsamados, and J. C. Stroeve, "Sea ice roughness overlooked as a key source of uncertainty in CryoSat-2 ice freeboard retrievals," *Journal of Geophysical Research: Oceans*, vol. 125, no. 5, p. e2019JC015820, 2020.
[57] L. Zhou, J. Stroeve, S. Xu, A. Petty, R. Tilling, M. Winstrup, P. Rostosky, I. R. Lawrence, G. E. Liston, A. Ridout *et al.*, "Inter-comparison of snow depth over arctic sea ice from reanalysis reconstructions and satellite retrieval," *The Cryosphere*, vol. 15, no. 1, pp. 345–367, 2021.
[58] S. Kacimi and R. Kwok, "Arctic snow depth, ice thickness and volume from ICESat-2 and CryoSat-2: 2018-2021," *Geophysical Research Letters*, p. e2021GL097448, 2022.
[59] P. Heil, C. Fowler, and S. Lake, "Antarctic sea-ice velocity as derived from ssm/i imagery," *Annals of Glaciology*, vol. 44, pp. 361–366, 2006.
[60] S. Schwegmann, C. Haas, C. Fowler, and R. Gerdes, "A comparison of satellite-derived sea-ice motion with drifting-buoy data in the weddell sea, antarctica," *Annals of Glaciology*, vol. 52, no. 57, pp. 103–110, 2011.
[61] S. Xu, L. Zhou, J. Liu, H. Lu, and B. Wang, "Data Synergy between Altimetry and L-Band Passive Microwave Remote Sensing for the Retrieval of Sea Ice Parameters—A Theoretical Study of Methodology," *Remote Sensing*, vol. 9, no. 10, p. 1079, 2017.
[62] M. Kern, R. Cullen, B. Berruti, J. Bouffard, T. Casal, M. R. Drinkwater, A. Gabriele, A. Lecuyot, M. Ludwig, R. Midthassel, I. Navas Traver, T. Parrinello, G. Ressler, E. Andersson, C. Martin-Puig, O. Andersen, A. Bartsch, S. Farrell, S. Fleury, S. Gascoin, A. Guillot, A. Humbert, E. Rinne, A. Shepherd, M. R. van den Broeke, and J. Yackel, "The Copernicus Polar Ice and Snow Topography Altimeter (CRISTAL) high-priority candidate mission," *The Cryosphere*, vol. 14, no. 7, pp. 2235–2251, 2020.
[63] M. Raspaud and M. Itkin, "SAR-Ice: A Sea Ice RGB Composite." [Online]. Available: https://custom-scripts.sentinel-hub.com/custom-scripts/sentinel-1/sar-ice/
[64] Y. LeCun, L. Bottou, Y. Bengio, and P. Haffner, "Gradient-based learning applied to document recognition," *Proceedings of the IEEE*, vol. 86, no. 11, pp. 2278–2324, 1998.
[65] L. Deng, J. Li, J.-T. Huang, K. Yao, D. Yu, F. Seide, M. Seltzer, G. Zweig, X. He, J. Williams *et al.*, "Recent advances in deep learning for speech research at Microsoft," in *2013 IEEE international conference on acoustics, speech and signal processing*. IEEE, 2013, pp. 8604–8608.
[66] Y. J. Kim, H.-C. Kim, D. Han, S. Lee, and J. Im, "Prediction of monthly Arctic sea ice concentrations using satellite and reanalysis data based on convolutional neural networks," *The Cryosphere*, vol. 14, no. 3, pp. 1083–1104, 2020.
[67] C. Durand, T. S. Finn, A. Farchi, M. Bocquet, G. Boutin, and E. Ólason, "Data-driven surrogate modeling of high-resolution sea-ice thickness in the Arctic," *The Cryosphere*, vol. 18, no. 4, pp. 1791–1815, 2024.
[68] J. Zhai and C. M. Bitz, "A machine learning model of Arctic sea ice motions," *arXiv preprint arXiv:2108.10925*, 2021.
[69] L. Hoffman, M. R. Mazloff, S. T. Gille, D. Giglio, C. M. Bitz, P. Heimbach, and K. Matsuyoshi, "Machine learning for daily forecasts of Arctic sea ice motion: An attribution assessment of model predictive skill," *Artificial Intelligence for the Earth Systems*, vol. 2, no. 4, p. 230004, 2023.
[70] M. Abadi, A. Agarwal, P. Barham, E. Brevdo, Z. Chen, C. Citro, G. S. Corrado, A. Davis, J. Dean, M. Devin, S. Ghemawat, I. Goodfellow, A. Harp, G. Irving, M. Isard, Y. Jia, R. Jozefowicz, L. Kaiser, M. Kudlur, J. Levenberg, D. Mané, R. Monga, S. Moore, D. Murray, C. Olah, M. Schuster, J. Shlens, B. Steiner, I. Sutskever, K. Talwar, P. Tucker, V. Vanhoucke, V. Vasudevan, F. Viégas, O. Vinyals, P. Warden, M. Wattenberg, M. Wicke, Y. Yu, and X. Zheng, "TensorFlow: Large-scale machine learning on heterogeneous systems," 2015, software available from tensorflow.org. [Online]. Available: https://www.tensorflow.org/